Draft version January 4, 2022
Typeset using LaTeX default style in AASTeX62

Radio Spectral Index Analysis of Southern Hemisphere Symbiotic Stars

John M. Dickey,[1] J. H. S. Weston,[2] J. L. Sokoloski,[3,4] S.D. Vrtilek,[5] and Michael McCollough[5]

[1] *School of Natural Sciences, Private Bag 37, University of Tasmania, Hobart, TAS, 7001, Australia*
[2] *Federated IT, 1201 Wilson Blvd, 27th Floor, Arlington VA 22209*
[3] *Astronomy Dept., Columbia University, New York, USA*
[4] *LSST Corporation, 933 N. Cherry Ave, Tucson, AZ 85721*
[5] *Harvard-Smithsonian Center for Astrophysics, 60 Garden Street, Cambridge, MA 02138, USA*

(Received 2 December 2020; Revised 27 January 2021)

ABSTRACT

Symbiotic stars show emission across the electromagnetic spectrum from a wide array of physical processes. At cm-waves both synchrotron and thermal emission is seen, often highly variable and associated with outbursts in the optical and X-rays. Most models of the radio emission include an ionized region within the dense wind of the red giant star, that is kept ionized by activity on the white dwarf companion or its accretion disk. In some cases there is on-going shell burning on the white dwarf due to its high mass accretion rate or a prior nova eruption, in other cases nuclear fusion occurs only occasionally as recurrent nova events. In this study we measure the spectral indices of a sample of symbiotic systems in the Southern Hemisphere using the Australia Telescope Compact Array. Putting our data together with results from other surveys, we derive the optical depths and brightness temperatures of some well-known symbiotic stars. Using parallax distances from Gaia Data Release 3, we determine the sizes and characteristic electron densities in the radio emission regions. The results show a range of a factor of 10^4 in radio luminosity, and a factor of 100 in linear size. These numbers are consistent with a picture where the rate of shell burning on the white dwarf determines the radio luminosity. Therefore, our findings also suggest that radio luminosity can be used to determine whether a symbiotic star is powered by accretion alone or also by shell burning.

Keywords: Symbiotic binary stars, White dwarf stars, Interacting binary stars, stellar accretion disks

1. INTRODUCTION

Mass-exchange binary stars demonstrate a tremendous diversity of emission processes. When one of the stars is a neutron star or black hole, the accretion process commonly produces hard X-rays as well as synchrotron emitting jets, similar to those seen in quasars, hence the term "micro-quasar" (Mirabel 1993). When the system contains a white dwarf with a red-giant companion, there is still a dramatic range of behavior observed, with the system often described as a symbiotic star (SySt) (Merrill 1941), see Munari (2019) for a recent review. The classification was originally based on the presence of optical spectral lines indicating a cool giant star mixed with very high ionization lines known at the time only in O stars and planetary nebulae. Since then symbiotic stars have demonstrated emission from the radio through to γ rays, often showing strong variability. Many of these properties are now identified with the accretion onto the white dwarf and the resulting shell burning, or nuclear fusion on the surface of the star. In some cases neutron star binaries are included in catalogs of SySts (Belczyński et al. 2000; van den Eijnden et al. 2018; Luna et al. 2013, type γ). Conditions in the red giant wind, and in particular its outflow velocity, can be determined from the optical spectrum, that often shows absorption lines or molecular bands such as TiO, H_2O, CO, CN and VO. These are in striking contrast to the high ionization species, e.g. [O VI] and other indicators of high temperature gas such as X-ray or γ ray emission (Giroletti et al. 2020). The X-ray spectrum can often distinguish between systems where the hot gas is in the boundary between the accretion disk and the white dwarf, on the surface of the white dwarf, or in a region where the winds from the two stars collide (Luna et al. 2013, δ, α, and β types, respectively), or the white dwarf fast wind collides with circumstellar material from an earlier, slower wind (Lucy et al. 2020).

Radio surveys of SySts were carried out in the 1980s and 90s, mostly with the NRAO VLA telescope (Seaquist, Taylor, and Button 1984; Seaquist and Taylor 1990, 1992; Seaquist et al. 1993; Ivison et al. 1995). Radio fluxes are collected in table 1 of Belczyński et al. (2000). More recently, individual sources have been monitored in the radio, particularly as target-of-opportunity projects to follow-up detections of outbursts in the optical and X-ray bands (Brocksopp et al. 2004; Lindford et al. 2019). In some cases the radio flux is highly variable on time scales as short as a few weeks (e.g. Lucy et al. 2020). There is good evidence from VLBI maps of transient radio jets that synchrotron emission is required, e.g. in R Aqr (Dougherty et al 1995), in CH Cyg (Crocker et al. 2001), and others (Rupen et al. 2008; Sokoloski et al. 2008; Giroletti et al. 2020), to explain the occasional short-lived jet emission seen after some optical and X-ray outbursts. The jets are typically found after optical outbursts (Sokoloski 2003, and references therein). Some SySts are recurrent novae, and SySt outbursts are similar in the radio to the emission from novae (e.g. Seaquist and Bode 2008; Weston et al. 2016), particularly in their mixture of rapidly brightening and fading non-thermal emission plus thermal emission with longer duration. Apart from these short-duration synchrotron outbursts, apparently most of the radio emission from SySts is thermal bremsstrahlung most of the time, as shown by the good correlation between radio luminosity and Hβ equivalent width (Seaquist, Taylor, and Button 1984, fig. 4).

One of the fundamental questions about SySts is whether or not there is shell burning, i.e. quasi-continuous nuclear fusion, on the surface of the white dwarf (Sokoloski et al. 2017). The radio luminosity can be a diagnostic for the energy input due to shell burning. Free-free (thermal) radio emission originates in gas that is either photo-ionized by the white dwarf continuum (Seaquist, Taylor, and Button 1984; Taylor and Seaquist 1984) or heated and ionized by a strong shock in the colliding wind region. If shell burning is happening on the white dwarf then both the ionizing radiation field and the wind power will be much stronger than if it is not, so the radio luminosity of the system should be stronger in systems with continuous nuclear fusion. To test this hypothesis, Weston (2016, chap. 5) selected a sample of SySts that show characteristics that indicate that they are powered by accretion and not by shell burning. These are sources that show UV flickering (rapid flux density variations caused by instabilities on the inner edge of the accretion disk) and X-ray spectra indicating that the source of the X-rays is either a colliding wind region [type β, Luna et al. (2013)] or the boundary layer between the accretion disk and the white dwarf star (type δ). Many of these were detected in Weston's radio survey, but with flux densities one to two orders of magnitude fainter than in surveys from 25 years earlier, that included all types of SySts.

As part of a radio-infrared-optical-UV-X-ray simultaneous survey of X-ray binaries, we observed several Southern Hemisphere SySts using the Australia Telescope Compact Array in June/July, 2007. The detected flux densities are similar to results of earlier studies (Ivison et al. 1995), but several of the sources changed in flux density over the 10 or more years since they were observed before. What is more useful is the spectral indices of the sources. Because the ATCA allows simultaneous observation in two bands (C- and X-band, at 4.8 and 8.64 GHz) separated by almost a factor of two in frequency, the spectral indices for our detections were measured with fairly good precision. In this paper we discuss the interpretation of the spectral index to determine the optical depth and brightness temperature of the emission regions. Since the SySts we observed now have Gaia eDR3 distances (Bailer-Jones et al. 2020), we can estimate the physical size as well as the solid angle of the ionized gas that emits the thermal radio emission. Comparing the results with similar quantities for the stars observed by Weston (2016) shows that the systems selected not to have shell burning are indeed very different from the rest.

2. RADIO OBSERVATIONS

The data were taken with the Australia Telescope Compact Array in the 6C configuration, that has 15 East-West baselines as shown on Table 1. The maximum projected baseline of 6 km is 1.7×10^5 λ at the highest observing frequency of 8.64 GHz giving minimum fringe separation of $1.1''$. The observations were taken over seven nights from 29 June - 5 July, 2007, in 12 hour sessions from 10-22^h LST. Two frequencies were observed simultaneously, centered on 8.64 and 4.80 GHz. The bandwidth was 128 MHz divided into 32 channels on each of two polarizations, i.e. correlator configuration full_128_2. The lowest andhighest four frequency channels are dropped to avoid filter edge effects, so the total effective bandwidth is 96 MHz at each frequency.

The primary flux and bandpass calibrator was 1934-638, observed every day, with secondary calibrators as shown on Table 1. Secondary calibrators were observed every 20 to 25 minutes, interspersed with two scans on SySt program source positions observed for eight minutes each. Solutions for antenna phases and gains were interpolated between successive calibrator scans and copied to the program source data, following the standard *MIRIAD* calibration process described in Sault et al. (1995). Calibrators were chosen within ∼20 degrees of the program source positions whenever

possible. Amplitude and phase errors were typically less than 5% and 5° as measured on the calibrators at 8.64 GHz. The weather was generally good with the exception of the first few hours of 30 June, when tropospheric effects cause rapid, intermittent phase changes for several hours.

Table 2 gives phase center positions for each program source, and upper limit flux densities for those that were not detected at 8.64 GHz. These were the most accurate positions available at the time, but the positions fitted to the cleaned maps are in some cases more precise. So we mapped and cleaned the field of view for each source, fitted the source position, then shifted the phase centers for all the *u,v* data to the new source position. We used the *MIRIAD* task UVFLUX to estimate the flux density on each day, based on the assumption of a point source at the phase center. The results are consistent with no flux variations over the seven nights of observing. We then put together all data to make maps, remove sidelobes with the CLEAN algorithm, and measure the position, flux density, and angular size by fitting a two dimensional Gaussian source moodel with task IMFIT.

Table 3 gives the measured quantities for each detected source at 8.64 and 4.80 GHz, based on the fitted Gaussian parameters: peak brightness (column 3), integrated flux density (column 4), position (columns 7 and 8), and angular diameter (column 9). All the sources are unresolved, or barely resolved by the beam, which is generally quite elliptical due to the sparse *u,v* coverage, typically ∼3.4″x 1.2″ at 8.64 GHz. The fitting program attempts to determine the source angular size, but this deconvolution fails if the fitted shape is consistent with the beam shape, within the errors on the major and minor axes of the fitted Gaussian. In that case the upper limit major axis given on Table 3 is the minor axis of the beam. The integral of the fitted Gaussian, that gives the flux density, is computed from the product of the fit results for the peak times the major and minor axes. It necessarily has a larger error than the peak value, and it is usually somewhat larger than the peak brightness, expressed as mJy/beam, due to the noise in the map, even for a source that is unresolved.

The conversion factor between mJy/beam and K of brightness temperature is ∼3.5 K/mJy at 8.64 GHz and ∼5 K/mJy at 4.8 GHz, depending on the beam size after tapering. For example, ESO 393-31 has peak value of 60 ± 1.2 mJy/beam at 8.64 GHz which gives peak brightness $T_B \simeq 210$ K. The actual brightness temperature may be higher by a factor of five or more, if the source solid angle is less than the beam solid angle, since the flux density is the

E-W Baseline Lengths	0.15 km	0.41 km	0.64 km
6C configuration	1.06 km	1.58 km	1.73 km
	1.99 km	2.14 km	2.63 km
	2.79 km	3.21 km	3.86 km
	4.27 km	5.85 km	6.00 km
Frequency Channels	32 x 4 MHz	(24 used)	

band center	4800	8640 MHz
resolution (FWHM)	1.8″ x 4″	1.2″ x 3.4″
Primary beam width	9.5′	5.3′
Calibration Sources	S_{4800} (in Jy)	S_{8640} (in Jy)
0537-441	3.9	5.3
0823-500	3.1	1.5
1059-63	1.1	1.4
1352-63	1.4	1.1
1514-241	3.0	3.0
1613-586	3.8	3.3
1730-130	4.1	3.6
1740-517	4.1	2.6
1741-038	5.8	5.7
1759-39	1.3	1.5
1921-293	9.5	10.9
1934-638	5.83	2.84

Table 1. Compact Array Telescope Parameters.

Source	RA	Dec	upper limit S_X (mJy)
RX Pup	8:14:12.31	-41:42:29.0	detected
KM Vel	9:41:14.00	-49:22:47.2	detected
V366 Car	9:54:43.29	-57:18:53.0	< 1.2
BI Cru	12:23:25.99	-62:38:16.1	detected
NSV 19500 = SS73 38[1]	12:51:26.21	-64:59:58.3	detected
ESO 390-7 = Hen 2-171	16:34:04.23[2]	-35:05:26.2[2]	< 1.0
NSV 20790 = AS 210	16:51:20.39	-26:00:26.8	detected
ESO 393-31 = PN H 1-36	17:49:48.17	-37:01:29.4	detected
IRAS 18015-2709 = SS73 122	18:04:41.28[2]	-27:09:13.6[2]	< 1.0
AN 68.1937 = V3929 Sgr	18:20:58.85[2]	-26:48:25.1[2]	< 1.5
RR Tel	20:04:18.54	-55:43:33.2	detected

Table 2. Observed Field Center Positions
[1]Alternate names are from table 1 of Belczyński et al. (2000).
[2]Positions were taken from SIMBAD. There are offset from the positions in Belczyński et al. (2000) of 8″for ESO 390-7, 19″for IRAS 18015-2709, and 7″for AN 68.1937.

brightness times the solid angle. In this case, IMFIT determines a source angular diameter of 0.9″. If the source solid angle, $\Omega = 1.13 \cdot (0.9)^2 \simeq 0.9$ arcsec^2 and the beam solid angle is 4.6 arcsec^2 = $1.13 \cdot 3.4'' \cdot 1.2''$, then the peak brightness is $T_B \sim 10^3$ K. (The factor of 1.13 comes from assuming Gaussian shape, for which the solid angle is 1.13 times the product of the major and minor axes, measured to the half-maximum points.) The analysis of the spectral index below in Section 3 predicts $T_B = 1.7 \pm 0.3 \cdot 10^3$ K assuming electron temperature $T_e = 10^4$ K. Reducing the assumed value of T_e to $\sim 6 \cdot 10^3$ K reduces the predicted brightness temperature to $T_B \simeq 10^3$ K, which matches the measured surface brightness if the source solid angle is $\Omega \simeq 0.9$(arc sec)^2.

Table 3 lists two components for NSV 19500 = SS73 38. The brighter component is at the star position, while the second component, which may be an unrelated source, is 53″ NW of the star. The probability of finding an extragalactic source with flux density of 1 mJy or greater in a circle of radius 53″ at 8.64 GHz is about 0.03 (Condon and Ransom 2016). At the eDR3 distance of 2.19 kpc the distance on the plane of the sky corresponding to 53″ is 0.6 pc.

3. ANALYSIS

Recent hardware upgrades to the VLA and ATCA telescopes provide increasedbandwidth which results in higher sensitivity (Perley et al. 2011; Wilson et al. 2011). Even the older receiver system on the ATCA used here was versatile in allowing observation with two bands simultaneously. Using the CX system with the new CABB receivers now allows many bands to be placed between about 4 and 10 GHz. This makes measurement of the spectral index, α, easier and more direct than in the original single-band VLA system that was used for the comprehensive surveys by Seaquist and collaborators, summarized by Ivison et al. (1995). The spectral index is important for interpretation of the radio continuum data, particularly thermal emission like that from most SySts. The discussion in this section follows the excellent textbook review of thermal radio emission by Condon and Ransom (2016, chap. 4).

The spectral index, α, can be defined at a single frequency as the slope of the flux density spectrum in log-log space, e.g. Seaquist, Taylor, and Button (1984, figure 6), but it is more commonly measured between two frequencies, ν_1 and ν_2 using the corresponding flux densities S_1 and S_2, by

$$\alpha = \frac{\log\left(\frac{S_1}{S_2}\right)}{\log\left(\frac{\nu_1}{\nu_2}\right)}. \quad (1)$$

With this definition thermal emission has α = +2, for the Rayleigh-Jeans (optically thick) black-body spectrum, decreasing to α = -0.1 for optically thin free-free emission. In the simplest case of a uniform slab of ionized gas with electron temperature, T_e, and density, n_e, the optical depth, τ, depends simply on frequency, ν, to the -2.1 power, as

$$\tau_\nu \; = \; C_1 \; \nu^{-2.1} \quad (2)$$

Source	Freq MHz	peak brightness mJy/bm	flux density mJy	RA (peak) J2000	Dec (peak) J2000	Maj ax ″
RX Pup	8640	24.4±0.6	30.0±1.1	8:14:12.30	-41:42:29.3	1.1
RX Pup	4800	25.3±0.5	27.9±0.8	8:14:12.31	-41:42:29.3	1.5
KM Vel	8640	3.3±0.1	3.3±0.3	9:41:14.00	-49:22:47.2	< 4
KM Vel	4800	2.6±0.5	2.6±0.7	9:41:13.99	-49:22:47.0	< 7
BI Cru	8640	4.0±0.2	4.3±0.3	12:23:25.97	-62:38:15.6	< 2
BI Cru	4800	4.6±0.2	5.0 ±0.4	12:23:25.98	-62:38:15.6	<3
NSV 19500 = SS73 38	8640	7.4±0.2	7.4±0.5	12:51:26.17	-64:59:57.7	<4
NSV 19500 = SS73 38	4800	5.2±0.3	5.0±0.4	12:51:26.19	-64:59:57.8	<4
Second source component:						
NSV 19500 b	8640	1.1±0.2	1.1±0.3	12:51:18.16	-64:59:53.9	<4
NSV 19500 b	4800	1.4±0.2	1.5±0.3	12:51:18.14	-64:59:53.9	<4
NSV 20790 = AS 210	8640	5.6±0.3	5.7±0.4	16:51:20.40	-26:00:26.7	< 3
NSV 20790 = AS 210	4800	4.9±0.5	5.7±0.9	16:51:20.40	-26:00:26.6	<3
ESO 393-31 = PN H 1-36	8640	60.0±1.2	65.5±1.8	17:49:48.21	-37:01:27.8	0.9
ESO 393-31 = PN H 1-36	4800	53.2±0.7	56.1±1.0	17:49:48.21	-37:01:27.8	0.9
RR Tel	8640	12.8±1.2	16.2±2.3	20:04:18.54	-55:43:32.9	<2
RR Tel	4800	15.3±0.5	17.6±0.8	20:04:18.54	-55:43:33.0	1.3

Table 3. Detected Source Properties

where the constant C_1 is the same at frequencies ν_1 and ν_2 as long as the emission at both frequencies comes from the same gas. This uniform slab assumption is obviously an over-simplification, but it allows us to derive representative numbers for the physical parameters by simple algebra, that otherwise might be buried in a more realistic gas dynamic and radiative transfer model. C_1 is given by

$$\frac{C_1}{(\mathrm{GHz})^{2.1}} \;=\; 3.28\cdot 10^{-7} \int \left(\frac{n_e}{\mathrm{cm}^{-3}}\right)^2 \left(\frac{T_e}{10^4\ \mathrm{K}}\right)^{-1.35} \frac{ds}{\mathrm{pc}} \;\simeq\; 3.28\cdot 10^{-7} \left(\frac{T_e}{10^4\ \mathrm{K}}\right)^{-1.35} \frac{EM}{\mathrm{cm}^{-6}\ \mathrm{pc}} \tag{3}$$

where the integral is taken along the line of sight, s, and the emission measure, EM, is the line of sight integral of the density squared: $EM \;=\; \int n_e^2\ ds$. If the emission at the two frequencies is from the same volume, then the spectral index is given by

$$\alpha = \frac{\log\left[\left(\frac{\nu_1}{\nu_2}\right)^2 \cdot \frac{1\ -\ exp(-C_1\ \nu_1^{-2.1})}{1\ -\ exp(-C_1\ \nu_2^{-2.1})}\right]}{\log\left(\frac{\nu_1}{\nu_2}\right)} \tag{4}$$

For a given pair of frequencies and the corresponding value of α, we can solve numerically for the value of C_1, giving the optical depth and hence the ratio of the brightness temperature, T_B, to T_e, since

$$T_{B,\nu} \;=\; T_e\ \left(1\ -\ e^{-\tau_\nu}\right) \tag{5}$$

where T_B and τ are functions of ν, easy to evaluate once C_1 is known.

For different geometries the constants vary, e.g. Mezger and Henderson (1967), Seaquist, Taylor, and Button (1984), and see the two component model in section A. The radiative transfer can be modeled for time-varying conditions, e.g. for an expanding sphere as in Wright and Barlow (1975) and Seaquist and Palimaka (1977). For the sake of simplicity, we continue with the uniform slab model to estimate representative values for the properties of the emission region based only on S_1 and α. If the ionized region has a sharp edge and uniform brightness temperature, then the flux density is

$$S_\nu \;=\; \frac{2\ k\ T_B\ \nu^2}{c^2}\ \Omega \;=\; \frac{T_B}{10^4\ \mathrm{K}}\ \ \frac{\Omega}{(\mathrm{arc\ \ sec})^2}\ \cdot \begin{cases} 539\ \mathrm{mJy}\ \ \text{at}\ \nu = 8.64\ \mathrm{GHz} \\ 585\ \mathrm{mJy}\ \ \text{at}\ \nu = 9.0\ \mathrm{GHz} \end{cases} \tag{6}$$

where k is Boltzmann's constant and c the speed of light. For a resolved source the solid angle, Ω, can be determined by deconvolving the beam shape, and the result depends on the size of the source; if the source is much smaller than the beam, then neither T_B nor Ω can be measured directly, only their product, i.e. $T_B\Omega = S_\nu\ c^2/(2\ k\ \nu^2)$.

Figure 1 illustrates the derivation of brightness temperature and solid angle (right hand panels) based on the measured value of α (upper left panel).

Precision in the measurement of α is critical. Propagating errors in equation 1 gives dispersion σ_α^2 where

$$\sigma_\alpha \;=\; \frac{S_2}{S_1}\ \frac{1}{\left|\ln\left(\frac{\nu_2}{\nu_1}\right)\right|}\ \sqrt{\frac{\sigma_{S_1}^2}{S_2^2}\ +\ \frac{S_1^2}{S_2^4}\ \sigma_{S_2}^2} \tag{7}$$

for an estimate of α based on measurements of S_1 and S_2 with their own dispersions of $\sigma_{S_1}^2$ and $\sigma_{S_2}^2$. The logarithmic term in the denominator shows that the two frequencies need to be separated by as large a factor as possible. Even with 10:1 signal to noise, i.e. $\frac{\sigma_S}{S} \sim 0.1$, the precision in α is marginal, $\sigma_\alpha \simeq 0.6$, for ν_1=4.8 GHz and $\nu_2 = 8.64$ GHz. If the frequency range is just 9.0 to 10.7 GHz as for the X-band system on the Karl Jansky Very Large Array then the error in α increases to 1.9. One of the advantages of the ATCA for this work is that its CX band allows a wide range of frequencies to be observed simultaneously.

In general several different sources of error contribute to the measurement of flux density, S, which complicates the determination of σ_α. Ordinary radiometer noise adds random numbers from a well-determined, Gaussian distribution that can usually be attenuated with longer integration. Random scale factors multiply the measured values by random numbers with a distribution that depends on the weather, the stability of the system, the observing strategy, and the level of flagging, i.e. rejection of data of mediocre quality. Generally the precision of flux densities measured at X-band ($\lambda \simeq 3.5$ cm) is 3% to 5%. If there are other radio sources within the primary beam then confusion can dominate the error in S; if the u,v coverage is sparse then the flux from the other sources will spread around the image plane as

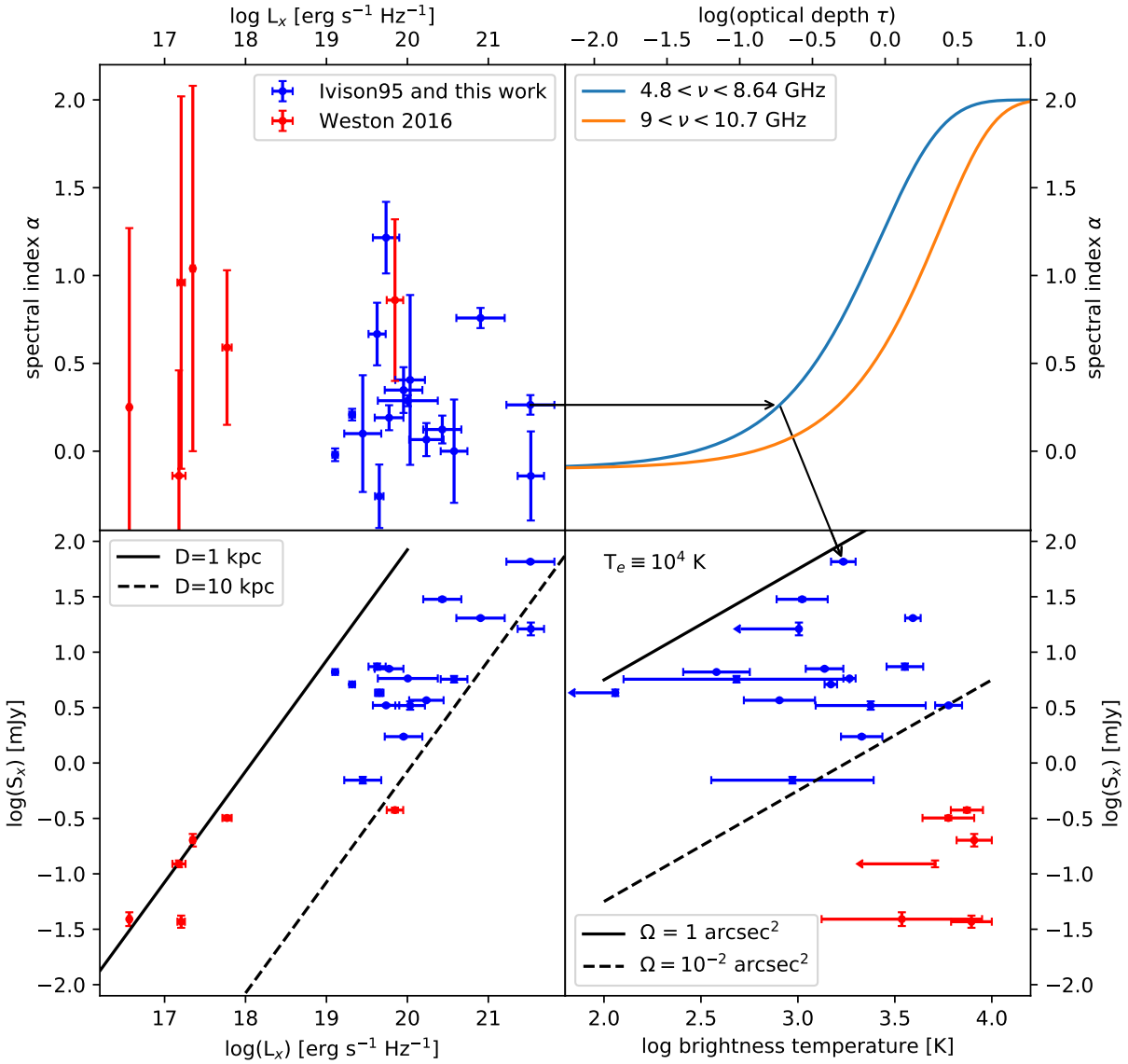

Figure 1. Spectral index analysis of radio detections. The lower left panel shows the distribution of flux densities at X-band, $S_X = S_\nu$ where $\nu = 8.64$ GHz for the values from Ivison et al. (1995) and this work, or ν=9.0 GHz for the values from Weston (2016), plotted vs. monochromatic luminosity, L_ν in units of erg s^{-1} Hz^{-1}. The luminosities are based on distances from Gaia eDR3 tabulated by Bailer-Jones et al. (2020).The upper left panel shows the corresponding values of the spectral index, α for each source. Based on the frequencies used to measure α, we find the corresponding value of optical depth from the curves on the upper right panel (equation 4). With the optical depth known we find the brightness temperatures shown in the lower right panel if we assume a value for the electron temperature, in this case T_e=10^4 K. Choosing a different value for T_e rescales the x-axis of the lower right panelby a factor of $\frac{T_e}{10^4\ K}$, and it scales the solid angles by the inverse, i.e. $\left(\frac{T_e}{10^4\ K}\right)^{-1}$ (see section A), since the flux density is the product of the brightness temperature times the solid angle in this simple geometry. The black arrows illustrate this strategy for one case (ESO 393-31). All points have error bars in both directions, but they are not plotted if the errors are smaller than the symbols.

noise-like fluctuations that limit the dynamic range of the image. In this experiment the primary beam is small enough that there are no bright confusing sources in the fields of the SySts at 4.8 and 8.64 GHz, but gain errors associated with weather are noticeable. For the source ESO 393-31 = PN H 1-36 these dominate the errors, but for the other

sources the flux densities are small enough that radiometer noise dominates. So we use the simple formula of equation 7 to determine σ_α, noting that these numbers may be underestimates.

Many SySts show parallax in the Gaia Data Release 3 (eDR3), Bailer-Jones et al. (2020).Although the resulting distance estimates come with fairly large error-bars for the more distant objects, the Gaia values are much more reliable than previous distance estimates, that were mostly based on photometry of the red giant star. Now we can convert flux to luminosity, and solid angle to projected area. Table 4 gives the resulting values, for the sample of stars observed in this study, and for those with eDR3 distances in the collection of Ivison et al. (1995) that have flux densities measured at $\lambda\lambda$ 3.5 and 6.25 cm, and for those with eDR3 distances in the survey of Weston (2016).

Column 1 of Table 4 gives the source name, column 2 gives the X-band flux density S_ν either at ν=8.64 GHz [from this work or Ivison et al. (1995)] or at ν=9.0 GHz [from Weston (2016)]. Column 3 shows the three eDR3 values: minimum, best, and maximum distance (D), in pc. We use the middle value for D to find the luminosity and source size. Column 4 gives the resulting luminosity, $L_X = 4\pi(D)^2 S_X$. Column 5 gives the measured value of α, with error, and column 6 gives the resulting value of τ at 8.64 GHz, or 9.0 GHz for the Weston (2016) sources. The values in the next five columns depend on the electron temperature in the emission region, here we take $T_e = 10^4$ K, but see section A for a discussion of how these change with changing T_e. Column 7 gives the $\log_{10}$ of the emission measure, EM, implied by τ. Using the Gaia distanceswe can determine the linear size from the solid angle, assuming some source geometry. We can get a characteristic number for the diameter, $d = (D)\sqrt{\frac{4}{\pi}\Omega}$ by assuming a simple cylinder of hot gas. The sizes, d, are given on column 10 of Table 4. If we assume that the line-of-sight depth is the same as d, then the electron density is given by $n_e = \sqrt{EM/d}$, given in column 11. For different values of the assumed electron temperature, d scales as $1/\sqrt{(T_e/10^4)}$ and n_e scales as $(T_e/10^4)^{0.25}$.

The brightest source detected in the 2007 observations is ESO 393-31 = PN H 1-36. It is classified as a SySt, but the radio emission is probably dominated by the extended ionized region of the associated planetary nebula. The prediction for $\Omega \simeq 0.8$ (arc sec)^2 is larger for this source than any of the others on Table 4 that have measured values of τ. (Three sources have only upper limits for τ, hence upper limits on T_B and lower limits on Ω.) As noted above, this source is marginally resolved, with deconvolved angular size $\sim$0.9″, giving $\Omega \simeq 0.9$ (arc sec)^2, in good agreement with the prediction.All the other derived values of Ω on Table 4 suggest angular diameters between 0.1″ and 1″ for the first group, i.e. those with flux densities S_X of a few mJy. At the eDR3 distances the linear diameters are a few hundred to a few thousand AU.The second group, those observed by Weston (2016) with flux densities of a few to a few tens of μJy, shows four sources, UV Aur, ZZ CMi, T Crb and ER Del, that have much smaller sizes with implied diameters $\sim$ 10 to 50 AU. Assuming that the power required to maintain the temperature and ionization in the emission regions is proportional to the collision rate and the total volume of ionized gas, i.e. $n_e^2 \cdot r^3$, then the first group of sources require about 100 times as much power as the four smaller, higher density sources in the second group based on the diameters and densities in columns 10 and 11 on Table 4.

The enigmatic system WRAY 151470, observed by Weston (2016) and listed on the last line on Table 4, is unlike either the high luminosity sources in the first group, or the low luminosity sources in the second group. On the left panels of Figure 1 this source stands out as the red point among the blue points on the right hand (high luminosity) side. This SySt was selected because of its high UV variability (Luna et al. 2013), but it does not have a δ or β/δ X-ray spectrum, nor does it have a high UV flux ratio (Weston 2016, pp. 148-149). Weston (2016, pp. 157-158) notes that WRAY 151470 therefore shows somewhat weaker evidence for being a purely accretion driven system than the other targets of that survey, and this anomalous behavior might be explained if there were some degree of shell burning present or if it were in a particularly active state. Based on its eDR3 distance, it now appears to fit better in the class of SySts with high radio luminosity, i.e. those above the line on Table 4.

The striking difference between the indicated sizes and densities of the ionized regions in the two groups of SySts supports the interpretation of Weston (2016) and Sokoloski et al. (2017) that the radio luminosity can distinguish between stars with shell burning and those without. Looking at the lower left panel of Figure 1 the wide range of radio luminosities, L_ν, is clear. None of the existing radio surveys has used a volume-limited sample, so we cannot begin to draw a luminosity function for the radio emission from SySts. But the distribution of points on the figure is suggestive of a bimodal luminosity function, with peaks around 10^{17} and 10^{20} erg s^{-1} Hz^{-1}. Interpreting these as the off- and on-states of shell burning in the SySts, these luminosity values may be useful for modelling the energetics of the ionized regions.

.

Source	S_X mJy	eDR3 D (kpc) min best max	$\log(L_X)$ erg s^{-1} Hz^{-1}	α_X	τ_X	log(EM) cm^{-6} pc	$T_{B,X}$ 10^3 K	$\log(\Omega)$ $(arcsec)^2$	diameter 10^2 AU	$\log(n_e)$ cm^{-3}
						— — —	estimates assuming $T_e=10^4$ K			— — —
RX Pup	30.0±1.1	2.22 2.74 3.60	20.43±0.24	0.12±0.08	0.11±0.04	7.50±0.14	1.1±0.4	-0.28±0.13	22±3	4.7±0.1
KM Vel	3.3±0.3	4.33 5.24 6.47	20.03±0.18	0.4±0.5	0.3±0.3	7.9±0.3	2.4±2.2	-1.6±0.3	9±3	5.1±0.3
BI Cru	4.3±0.3	2.75 2.96 3.14	19.65±0.05	-0.26±0.18	< 0.01	< 6.5	< 0.1	> -0.2	> 28	< 4.2
NSV 19500	7.4±0.5	1.91 2.19 2.47	19.63±0.11	0.67±0.18	0.44±0.14	8.09±0.12	3.6±0.9	-1.41±0.09	4.8±0.5	5.4±0.1
NSV 20790	5.7±0.4	6.10 7.44 9.00	20.58±0.17	0.0±0.3	0.05±0.15	7.1±0.6	0.5±1.4	-0.7±0.6	39±19	4.4±0.5
ESO 393-31	65.5±1.8	4.72 6.50 9.15	21.5±0.3	0.26±0.06	0.19±0.03	7.73±0.07	1.7±0.3	-0.15±0.06	62±4	4.62±0.05
RR Tel	16.2±2.3	10.6 13.2 15.9	21.53±0.16	-0.14±0.25	< 0.11	< 7.5	< 1.0	> -0.5	> 81	< 4.4
V835Cen	5.8±0.1	2.78 3.83 5.86	20.0±0.4	0.29±0.03	0.20±0.02	7.76±0.04	1.8±0.1	-1.24±0.03	10.4±0.4	5.03±0.03
He 2-127	0.7±0.1	4.16 5.79 7.54	19.45±0.23	0.1±0.3	0.10±0.18	7.4±0.5	0.9±1.5	-1.9±0.4	7.7±2.9	4.9±0.3
AG Peg	6.6±0.1	1.22 1.27 1.32	19.11±0.03	-0.02±0.04	0.04±0.02	7.0±0.2	0.4±0.2	-0.49±0.17	8.2±1.5	4.7±0.1
He 2-38	1.7±0.1	5.15 6.59 8.61	19.95±0.23	0.35±0.13	0.24±0.08	7.83±0.12	2.1±0.6	-1.82±0.11	9.1±1.1	5.1±0.1
SS 38	5.1±0.1	1.77 1.84 1.92	19.32±0.04	0.21±0.03	0.16±0.01	7.65±0.04	1.5±0.1	-1.19±0.03	5.3±0.2	5.12±0.03
He 2-104	3.3±0.1	3.10 3.71 4.48	19.74±0.16	1.2±0.2	0.9±0.3	8.41±0.12	6.0±1.0	-1.99±0.07	4.2±0.3	5.5±0.1
HD149427	20.3±0.5	3.69 5.75 8.10	20.9±0.3	0.76±0.06	0.50±0.06	8.15±0.05	3.9±0.4	-1.02±0.04	20.1±0.9	5.08±0.04
He 2-176	3.7±0.1	4.79 6.25 7.98	20.23±0.21	0.07±0.09	0.08±0.05	7.4±0.2	0.8±0.4	-1.1±0.2	21±4	4.7±0.1
K3-9	7.1±0.2	2.31 2.65 3.25	19.77±0.18	0.19±0.07	0.15±0.04	7.62±0.11	1.4±0.3	-1.02±0.10	9.3±1.0	4.98±0.08
UV Aur	0.20±0.03	0.94 0.96 0.99	17.35±0.02	1.0±1.0	1.7±8.2	8.7±0.8	8.1±1.9	-3.37±0.09	0.22±0.02	6.3±0.3
ZZ CMi	0.32±0.02	1.18 1.25 1.33	17.77±0.06	0.6±0.4	0.9±0.8	8.4±0.3	6.0±2.1	-3.04±0.13	0.42±0.06	6.1±0.4
NQ Gem	0.12±0.01	0.94 1.01 1.11	17.18±0.08	-0.1±0.6	< 0.7	< 8.3	< 5	> -3.4	> 0.23	< 6.1
T CrB	0.04±0.01	0.86 0.89 0.91	16.56±0.02	0.3±1	0.4±1.8	8.1±0.7	3.4±5.5	-3.7±0.4	0.14±0.05	6.1±0.2
ER Del	0.04±0.01	1.81 1.90 2.01	17.20±0.05	1.0±1.1	1.5±8.4	8.7±0.8	7.9±2.1	-4.09±0.10	0.19±0.02	6.4±0.3
WRAY151470	0.38±0.02	10.7 12.5 14.1	19.85±0.10	0.9±0.5	1.4±0.9	8.6±0.2	7.4±1.6	-3.06±0.08	4.1±0.4	5.7±0.3

Table 4. Results for the physical parameters of the emission regions based on the spectral index analysis described in equations 2 - 7.

4. FUTURE OBSERVATIONS

The results of the analysis above show the importance of accurate measurement of the spectral index, α, for the interpretation of radio emission from SySts. A more sophisticated approach would be to measure the fluxes over a range of frequencies, if possible covering a factor of 3 to 5 in ν centered near 8 GHz, where most of the sources are becoming optically thin. This may require switching receivers at short intervals so that the u,v coverage is nearly identical, in case of source structure or confusing sources in the primary beam. Repeat observations in different telescope configurations will be needed if the emission is strongly resolved. Given four or five accurate measurements of S_ν from about 4 to 16 GHz, spectral indices and optical depths could be determined with good precision.If the conditions in the emission region are not uniform, then the shape of the radio spectrum in this frequency range could allow separation of components with different values of τ (section A).

One of the most interesting parameters to measure is the electron temperature, T_e, in the emission region, that is used in this analysis to translate from optical depth to brightness temperature. On Table 4 we use $T_e = 10^4$ K which is somewhat higher than in most HII regions, but lower than in planetary nebulae (Zhang et al. 2004). It is possible that some of the ionized gas seen in the radio is much hotter, see section A. The X-ray emission is thermal in all well studied SySts, with implied temperatures as high as 10^7 K ~ 1 keV (for β-type systems, see Luna et al. (2013)). The white dwarf stars have surface temperatures in the range $2{\cdot}10^4$ to $3{\cdot}10^5$ K (Contini et al. 2009). The temperature in the colliding wind region of AG Peg has been determined spectroscopically by Nussbaumer et al. (1995) as $T_e \simeq 2{\cdot}10^4$ K and density in the range 10^7 to 10^{10} cm^{-3}, much higher than the densities implied by the radio emission assuming $T_e = 10^4$ K, (Table 4, column 11). The cleanest way to determine the electron temperature in the radio emission region is to use the line-to-continuum ratios of H recombination lines with quantum levels $n \sim 80$ to 100 as has been done for HII regions (Brown et al. 2017; Wenger et al. 2019). This takes long integrations even for sources with $S_X \sim 100$ mJy. For measurements of radio recombination lines in SySts we may have to wait for the Next Generation VLA telescope (Balser et al. 2018) and the Square Kilometre Array (O'Brien et al. 2015).

Direct measurement of the sizes of the emission regions in more SySts would be very helpful. VLBI studies such as the recent combined EVN-VLBA monitoring of V 407 Cyg by Giroletti et al. (2020) have surface brightness sensitivity limited to $T_B > 10^5$ K, so they mostly show the distribution of non-thermal emission, although if some of the radio flux comes from the X-ray emission region it might be remotely possible that in a few very high density clumps the brightness temperature could be high enough to detect their thermal emission with VLBI. But thermal emission from regions with sizes on the order of 10^{-1} arc sec could be measured at higher frequencies with ALMA or the JVLA, or possibly with the ATCA.

Monitoring S_X from a number of SySts of both high and low radio luminosities with a cadence of a few weeks to months with photometric precision of 5% or better would be of interest. The recombination time for gas at $T_e \sim 10^4$ K and $n_e \sim 10^5$ cm^{-3} is about 460 days, for $n_e \sim 10^6$ cm^{-3} it is 46 days (Draine 2011, case B, fig 14.1), thus the lower luminosity sources would be most likely to show flux variations on time scales of a few weeks to months.

5. CONCLUSIONS

Based on the numbers in column 4 of Table 4 and the lower left panel of Figure 1, a dividing line between burning and non-burning white dwarf stars in symbiotic binaries is given by X-band (8.6 GHz) luminosity $\log_{10}(L_X) \sim 18.5$. SySts with monochromatic luminosity (in erg s^{-1}Hz^{-1}) above $10^{18.5}$ can ionize an HII region with size of 400 to 6000 AU. These ionized regions almost qualify as ultracompact HII regions (Churchwell 1990, Table 2), that typically have emission measures between 10^7 and 10^9 pc cm^{-6} and sizes $\sim 5 \cdot 10^{-3}$ up to $\sim$0.1 pc. Unlike ultracompact HII regions, the radio bright SySts are buried in a red giant wind rather than a molecular cloud, and they may not be entirely photoionized but instead or in addition they may be heated and ionized by a colliding-wind shock. The low radio luminosity SySts (UV Aur, ZZ CMi, T Crb and ER Del) have higher emission measures, but much smaller implied diameters, than the high radio luminosity systems. Either the colliding-wind shock is much closer to the white dwarf, and/or the star produces many fewer ionizing photons. Further observations as suggested in Section 4 may reveal which process, or how much of each, is responsible for the ionized gas.

This research has made use of of NASA's Astrophysics Data System; the SIMBAD database and VizieR catalogue access tool, CDS, Strasbourg, France; and matplotlib for python (Hunter 2007).

J.L.S. was supported by NSF award AST-1616646.

This research was supported in part by the Australian Research Council grants DP0770157 and DP0559613.

The authors are grateful to the referee for thorough and helpful reviews of the manuscript.

The Australia Telescope Compact Array is part of the Australia Telescope National Facility which is funded by the Australian Government for operation as a National Facility managed by CSIRO.

This work has made use of data from the European Space Agency (ESA) mission *Gaia* (https://www.cosmos.esa.int/gaia), processed by the *Gaia* Data Processing and Analysis Consortium (DPAC, https://www.cosmos.esa.int/web/gaia/dpac/consortium). Funding for the DPAC has been provided by national institutions, in particular the institutions participating in the *Gaia* Multilateral Agreement.

REFERENCES

Bailer-Jones, C.A.L., Rybizki, J., Fouesneau, M., Demleitner, M., and Andrai, R., 2021, AJ in press, see arXiv:2012.05220. Data served by https://dc.zah.uni-heidelberg.de/gedr3dist/q/cone/form

Balser, D.S., Anderson, L.D., Bania, T.M., Dickey, J.M., Roshi, D.A., et al., 2018, in *Science with a Next-Generation Very Large Array*, ed. Eric J. Murphy, ASP Conference Series, Monograph 7, pp. 431-439.

Belczyński, K., Mikołajewska, J., Munari, U., Ivison, R.J., Friedjung, M., 2000, A&AS, 146, 407.

Brocksopp, C., Sokoloski, J.L., Kaiser, C., Richards, A.M., Muxlow, T.W.B, and Seymour, N., 2004, MNRAS, 347, 430.

Brown, C., Jordan, C., Dickey, J.M., Anderson, L.D., Armentrout, W.P., et al. 2017, AJ, 154, 23B.

Churchwell, E., 1990, Astron. Astroph. Review, 2, 79.

Condon, J.J. and Ransom, S.M., 2016, *Essential Radio Astronomy*, (Princeton: Princeton University Press) see https://www.cv.nrao.edu/~sransom/web/xxx.html

Contini, M. Angeloni, R., and Rafanelli, P., 2009, MNRAS, 396, 807.

Crocker, M.M., Davis, R.J., Eyres, S.P.S., Bode, M.F., Taylor, A.R., Skopal, A. and Kenny, H.T., 2001, MNRAS, 326, 781.

Dougherty, S. M., Bode, M. F., Lloyd, H. M., Davis, R. J., and Eyres, S. P. 1995, MNRAS, 272, 843.

Draine, B.T., 2011, *Physics of the Interstellar and Intergalactic Medium*, [Princeton: Princeton University Press].

Giroletti, M., Munari, U., Körding, E., Mioduszewski, A., Sokoloski, J., et al., 2020, A&A, 638, A130.

Hunter, J. D. 2007, Computing In Science & Engineering, 9, 90

Ivison, R.J., Seaquist, E.R., Schwarz, H.E., Hughes, D.H., and Bode, M.F., 1995, MNRAS, 273, 517.

Lindford, J.D., Chomiuk, L., Sokoloski, J.L., Weston, J.H.S., van der Horst, et al. 2019, ApJ, 884:8.

Lucy, A.B., Sokoloski, J.L., Munari, U., Roy, N., Kuin, N.P.M., et al. 2020, MNRAS, 492, 3107.

Luna, G.J.M., Sokoloski, J.L., Mukai, K., and Nelson, T., 2013, A&A, 559, A6.

Merrill, P. 1941, Popular Astronomy 49, 113.

Mezger, P.G. and Henderson, A.P., 1966, ApJ, 147, 471.

Mirabel, I.F. 1993, Recherche 24, 746.

Munari, U. 2019, in *The Impact of Binaries on Stellar Evolution* Eds Beccari, G. and Boffin, H.M.J. [Cambridge: Cambridge University Press] arXiv:1909.01389v1.

Nussbaumer, H., Schmutz, W., and Vogel, M., 1995, A&A, 293, L13.

O'Brien, T., Rupen, M., Chomiuk, L., Ribeiro, V., Bode, M., et al., 2015, in *Advancing Astrophysics with the Square Kilometre Array* Proceedings of Science (AASKA14) 062.

Perley, R.A., Chandler, C.J., Butler, B.J., Wrobel, J.M., ApJL, 739, L1.

Rupen, M.P., Mioduszewski, A.J., and Sokoloski, J.L., 2008, ApJ, 688, 559.

Sault, R.J. and Teuben, P.J. and Wright, M.C.H., 1995, in *Astronomical Data Analysis Software and Systems IV*, eds. R. Shaw, H.E. Payne, J.J.E. Hayes, ASP Conference Series, 77, 433. https://www.atnf.csiro.au/computing/software/miriad/

Seaquist, E. R., and Bode, M. F. 2008, in Classical Novae, 2nd Edition, ed. M. F. Bode and A. Evans (Cambridge: Cambridge University Press), 141-166.

Seaquist, E.R., Krogulec, M., Taylor, A.R., 1993, ApJ, 410, 260.

Seaquist, E.R. and Palimaka, J., 1977, ApJ, 217, 781.

Seaquist, E.R. and Taylor, A.R., 1990, ApJ, 349, 313.

Seaquist, E.R. and Taylor, A.R., 1992, ApJ, 387, 624.

Seaquist, E.R., Taylor, A.R., and Button, S., 1984, ApJ, 284, 202.

Sokoloski, J.L., 2003, Journal of the American Association of Variable Star Observers, 31, 89.

Sokoloski, J.L., Rupen, M.P., and Mioduszewski, A.J., 2008, ApJL, 685, L137.

Sokoloski, J.L., Lawrence, S., Crotts, A.P.S., and Mukai, K., 2017, in *Accretion Processes in Cosmic Sources APCS2016*, Proceedings of Science (arXiv:1702.05898v1).

Taylor, A.R. and Seaquist, E.R., 1984, ApJ, 286, 263.

van den Eijnden, J., Degenaar, N., Russell, T.D., Miller-Jones, J.C.A., Wijnands, R., et al. 2018, MNRAS, 474, L91.

Wenger, T. V., Dickey, J.M., Jordan, C.H., et al. 2019, ApJS, 240, 24.

Weston, J.H.S., Sokoloski, J.L., Chomiuk, L., Linford, J.D., Nelson, T., et al., 2016, MNRAS, 460, 2687.

Weston, J.H.S. 2016, *Radio Observations as a Tool to Investigate Shocks and Asymmetries in Accreting White Dwarf Binaries* Ph. D. Thesis, Columbia University. https://doi.org/10.7916/D87M082M

Wilson, W. E., Ferris, R. H., Axtens, P., et al. 2011, MNRAS, 416, 832

Wright, A.E. and Barlow, M.J., 1975, MNRAS, 170, 41.

Zhang, Y., Liu, X.-W., Wesson, R., Storey, P.J., Liu, Y. and Danziger, I.J., 2004, MNRAS, 351, 935.

APPENDIX

A. MAKING THE SOURCE MODEL MORE REALISTIC

,

A.1. *Varying the Electron Temperature*

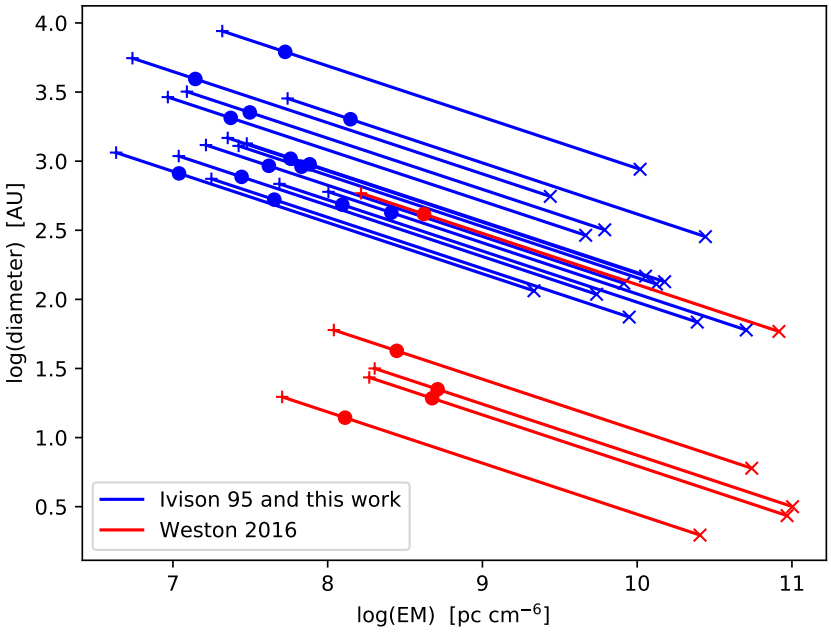

Figure 2. Variation of the derived values of emission measure, EM, and diameter with T_e, the assumed electron temperature. The circles correspond to the points on figure 1 and Table 4, with $T_e = 10^4$ K. The lines show how those points would move for $5 \cdot 10^3 < T_e < 5 \cdot 10^5$ K. Decreasing T_e by a factor of two reduces the derived value for EM and increases the diameter, thus moving the point left and up to the + position, while increasing T_e by a factor of 50 moves the point down and to the right as indicated by the $\times$ symbol.

One of the many interesting features of SySts' radio emission is the possibility that it may come from regions of relatively high electron temperature, T_e, as discussed in section 4. Changing the assumed value of T_e changes both the emission measure, EM, derived from C_1 in equation 3, as well as the brightness temperature derived by equation 5 and the resulting values of Ω, d, and n_e. The derived values of density and size change with T_e as shown on figure 2. For each of the sources on Table 4 the circle on figure 2 shows the derived values of EM and the log of the diameter (columns 7 and 10), with lines showing how these values would change depending on the assumed value of T_e. Decreasing T_e to $5 \cdot 10^3$ K would move the points up and to the left on the figure to the locations marked by + symbols, while increasing T_e to $5 \cdot 10^5$ K moves the points down and to the right as indicated by the $\times$ symbol. The implied density $n_e \propto \sqrt{EM/d}$ increases as the electron temperature increases.

The sources on Table 4 include X-ray sources of types α, β, δ, and β/δ in the classification system of Luna et al. (2013). Type β, for which the X-rays originate in a region of collision between winds from the white dwarf and the red giant star, are most likely to show a correspondence between the ionized gas regions emitting the radio and X-rays. These include RX Pup, BI Cru, AG Peg, He 2-104, UV Aur, ZZ CMi, and NQ Gem. Whether or not these show higher electron temperatures in the radio is a question that will require combined modelling of data taken in the radio and X-ray bands simultaneously.

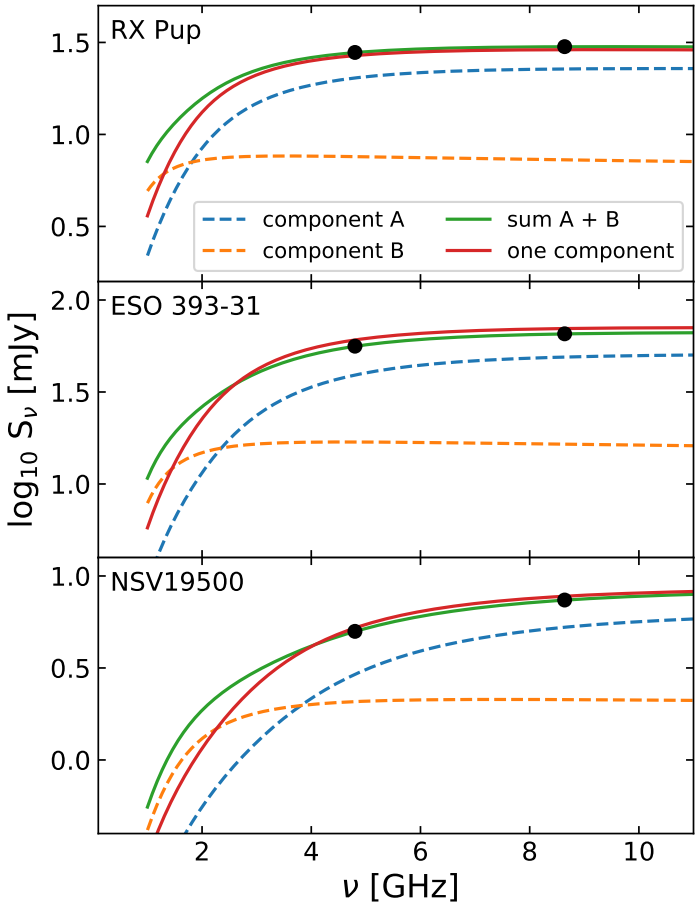

Figure 3. Two component models of the density distribution. The spectra in the top panel are for the low optical depth source, RX Pup ($\tau \simeq 0.11$). The middle panel shows spectra for the intermediate optical depth source ESO 393-31 ($\tau \simeq 0.19$). The bottom panel shows spectra for the higher optical depth source NSV 19500 = SS 73 38 ($\tau \simeq 0.44$). The black dots show the measured flux densities at 4.8 and 8.64 GHz that constrain the model parameters. The solid red curve is the best fit single component fit, as given on Table 4, and as EM_1 on Table 5. The dashed lines show the contribution from the two components separately, and the solid green line is their sum.

A.2. *Two Components with Different Emission Measures*

The results on table 4, columns 6 - 11, assume a cylindrical geometry for the source, so that the emission measure has the same value for all lines of sight through the ionized gas. This assumption allows derivation of representative values for the physical parameters of the source, but it is far from realistic as a density distribution. A somewhat more robust model would allow the emission measure to vary with position, e.g. in a core-halo structure that might represent an ionized wind around a central high density region. Since almost all SySts are unresolved by the ATCA, we cannot separate the contributions of the different regions to the overall emission sprectrum. But we can get a rough idea of the variation in the physical parameters for a more complex density structure by making a two-component model of the emission measure, EM, and the solid angle, Ω.

If we assume that the emission from the source comes from two regions, one (component A) with emission measure ten times greater than the other (component B), but with solid angle just one third as large, then we can make an estimate of how much the results on Table 4 would have to change. These ratios of $\frac{EM_A}{EM_B} = 10$ and $\frac{\Omega_A}{\Omega_B} = \frac{1}{3}$ mean that at low frequencies, where both components are optically thick, the emission comes mostly (75%) from component B,

but at high frequencies where both components are optically thin, the emission comes mostly (77%) from component A, since its optical depth and hence brightness temperature will be ten times higher than T_B in region B. At the X-band frequencies of this study, most sources are in between these two limits, as illustrated on figure 3. Given the two measured flux densities at two frequencies (4.8 and 8.64 GHz), and the two assumed ratios for EM and Ω between the two components, we can solve a system of four simultaneous equations to find both values of emission measure, EM_A and EM_B, both values of solid angle, Ω_A and Ω_B, and from these the values of all the other parameters on Table 4 for both components.

Shown on figure 3 are three sources with quite different values of α between 4.8 and 8.64 GHz: RX Pup that is very optically thin ($\alpha \simeq 0.11$), ESO 393-31 that is moderately optically thin ($\alpha \simeq 0.19$), and the higher optical depth source NSV 19500 = SS 73 38 ($\alpha \simeq 0.44$).Spectra for the two components (A and B) are shown on each panel, their sum spectrum is shown, and for comparison the single component spectrum corresponding to the values from table 4. The corresponding results for components A, B, and the one component model (1) are summarized on table 5 for the three sample stars.

Star	RX Pup	ESO 393-31	NSV 19500
$\log_{10}(EM_A)$	7.6	7.9	8.3
$\log_{10}(EM_B)$	6.6	6.9	7.3
$\log_{10}(EM_1)$	7.5	7.7	8.1
$\log_{10}(\Omega_A)$ arcsec^2	-0.5	-0.4	-1.7
$\log_{10}(\Omega_B)$ arcsec^2	-0.04	+0.08	-1.2
$\log_{10}(\Omega_1)$ arcsec^2	-0.3	-0.1	-1.4
τ_A (8.64 GHz)	0.15	0.26	0.71
τ_B (8.64 GHz)	0.015	0.026	0.071
τ_1 (8.64 GHz)	0.11	0.19	0.44
diameter d_A (AU·10^2)	17	46	3.4
diameter d_B (AU·10^2)	30	80	5.9
diameter d_1 (AU·10^2)	22	62	4.8
$\log_{10}(n_{e,A})$	4.9	4.8	5.5
$\log_{10}(n_{e,B})$	4.1	4.1	4.9
$\log_{10}(n_{e,1})$	4.7	4.6	5.4

Table 5. Physical parameters of the two component emission model, compared with the one component results, for the three representative sources illustrated on figure 3. The units of EM are pc cm^{-6} and n_e is in cm^{-3}.

The two component results shown on table 5 are typically different by factors of three to six, except for the emission measures, that are forced to have a ratio of ten, and the optical depths, that must also differ by a corresponding factor of ten. In most cases the one component results are roughly the geometric mean of the results for components A and B, thus different from each by about a factor of two. Although we can imagine that component B would be concentric with component A, as a halo around the higher density core, that is not assumed here. As long as they are both contained within the beam, their juxtaposition does not matter. The result of this analysis is to suggest that a factor of three variation in the sizes and electron densities on table 4 might be expected due to source structure, but a factor of ten or more would be unlikely.Of course, other source components, e.g. a low density wind, that do not contribute significantly to the flux at either frequency, are not constrained by these observations.

A.3. *Spatial Structure of the Electron Density*

The values on the last five columns of table 4 assume not only that $T_e = 10^4$ K but also that the density distribution is a uniform cylinder, with length along the line of sight, s, equal to its diameter, d, so that the emission measure is simply $EM = n_e^2 d$ that is found from C_1 by equation 3. For a sphere of uniform density the EM changes with position, from a peak at the center, to zero at the edge, as $EM(b) = n_e^2\sqrt{(d)^2 - (2b)^2}$ with b the impact parameter, or minimum distance from the center to the line of sight. Averaged over the solid angle of the source, the mean EM of a sphere is $\langle EM \rangle = \frac{2}{3}\, d\, n_e^2$. For an unresolved source with a given value of C_1 (derived from the measured value of

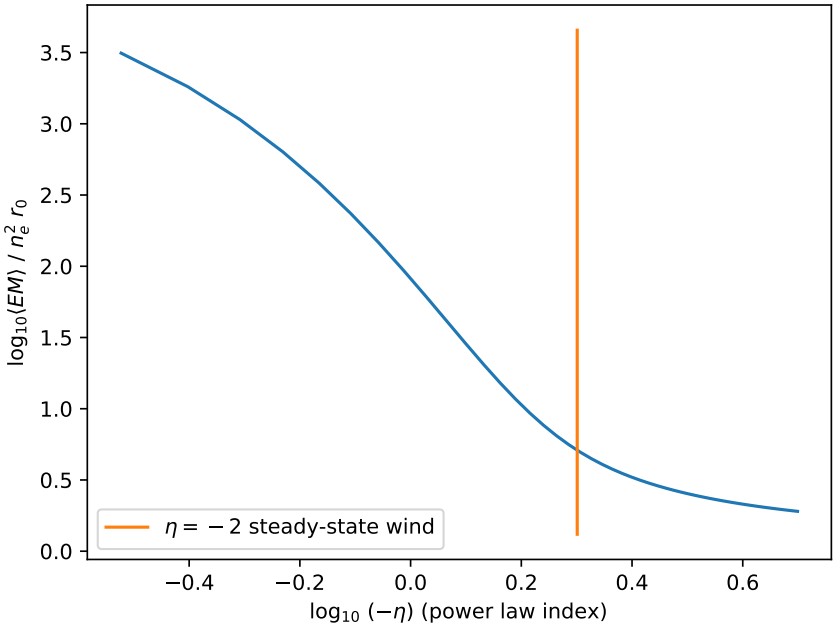

Figure 4. Variation of the mean emission measure $\langle EM \rangle$, equation A2, with the power law index, η, of a steady-state wind, equation A1. For a cylinder $\langle EM \rangle = n_e^2\ d$, for the steady-state wind $\langle EM \rangle \simeq 5.1\ n_0^2\ r_0$.

α by equation 4), the sphere has lower $\langle EM \rangle$ than the cylinder by a factor of 2/3. So to explain the observed α the diameter must by larger than the value on table 4, column 10 by a factor of 1.5, or the density must by larger than the value in column 11 by a factor of 1.22.

A more realistic distribution of n_e in the SySt environment is a steady state wind, with constant velocity and mass-loss rate, so that the density is

$$\frac{n_e}{n_0} \ = \ \left(\frac{r}{r_0} \right)^{\eta} \tag{A1}$$

with power law index $\eta = -2$. The wind starts at radius r_0, within which the density is a constant, n_0. The mass and solid angle diverge for this wind, but the flux density and the solid angle average of the emission measure are finite. Integrating n_e^2 along lines of sight, $\int ds$, at a range of values for b gives

$$\langle EM \rangle \ = \ \frac{\int \ 2\pi b \left[\int \ n_e^2(b,s) ds \ \right] \ db}{\pi r_0^2} \ \simeq \ 2.6\ n_0^2\ d \tag{A2}$$

where $d = 2r_0$ and $n_e(b,s) = n_e(r)$ given by equation A1 with $r = \sqrt{b^2 + s^2}$, and s is the line of sight distance from the point of closest approach to the center ($s = 0$). For the $\eta = -2$ wind, $\langle EM \rangle$ is increased relative to the hard-edge sphere by a factor of about 3.8, and relative to the cylinder with diameter d the wind has $\langle EM \rangle$ higher by a factor of $\sim$2.6. This would lead to values for d lower by a factor of 2.6 relative to the numbers on table 4, column 10, or values for n_e lower by $\sqrt{2.6} \simeq 1.6$, i.e. a decrease of 0.2 in $\log_{10}(n_e)$ on column 11 or a combination of a smaller change in both quantities.

For different power-law indices η in equation A1 the $\langle EM \rangle$ varies with η as shown in figure 4. The special case of a steady-state, constant velocity wind ($\eta = -2$) is indicated by the vertical line. Other values of η require either acceleration/deceleration of the wind, e.g. due to a shock, which is typical of SySts with X-ray spectra of type β (Luna et al. 2013), or variations in the mass loss rate with time, as is seen in the radio emission shortly after a nova outburst (e.g. Weston et al. 2016). More comprehensive and informative models for the radio emission regions of SySts take into account the rich detail of the optical, IR, and X-ray spectra as well as long and short term changes in their luminosity in all bands (e.g. Contini et al. 2009).

The density models discussed in this section allow simple integration of n_e^2 to compute the mean emission measure, $\langle EM \rangle$, that is derived from α by equations 3 and 4 for an unresolved source. If the sources were well resolved by the telescope, then the computation would be much more complicated, because the source might be optically thin in some parts ($\alpha \simeq -0.1$), optically thick in others ($\alpha \simeq +2$). For those limiting values, the error in a measurement of α leads to a very large error in τ, and the derived value of the EM is very imprecise, i.e. the horizontal parts of the curves in the upper right panel of figure 1. The point of the calculations in this section is that, for unresolved sources where α and hence τ are fairly well determined, the resulting $\langle EM \rangle$ and hence the size and density of the emission region are close to the values given by the uniform cylinder model (Table 4).